

## Article

# Validation for Aerodynamic Performance on Over-Expanded State of Single Expansion Ramp Nozzle Configuration

Ye Chen <sup>1</sup>, Zhongxi Hou <sup>1</sup>, Bingjie Zhu <sup>1</sup>, Zheng Guo <sup>1,\*</sup> and Boting Xu <sup>2</sup>

<sup>1</sup> College of Aerospace Science and Engineering, National University of Defense Technology, Changsha 410073, China

<sup>2</sup> Consulting Center for Strategic Assessments, Academy of Military Sciences, Beijing 100091, China

\* Correspondence: guozheng@nudt.edu.cn

**Abstract:** The performance of a single expansion ramp nozzle (SERN) drastically declines on over-expanded conditions. A numerical code can accurately predict nozzle performance in the over-expanded state, which is crucial for the SERN configuration design. A Reynolds-averaged Navier–Stokes (RANS) simulation of the SERN jet in an over-expanded state was performed to verify the numerical performance of the well-established commercial CFD solver (ANSYS Fluent™ v202) and rhoCentralFoam solver in OpenFOAM. The wall pressure distributions and flow field characteristics including the shock structures and the width of the jet were studied in detail with an inlet nozzle pressure ratio (NPR) of 1.5, 3, 4, and 8. The SERN aerodynamic performance with an inlet NPR ranging from 1.5 to 9 was then calculated. The results showed that the Fluent 3D simulation could qualitatively predict the characteristics of the internal and external flow of the nozzle, because it overestimated the wall pressure and shock wave position. Two-dimensional (2D) simulations made it difficult to capture the external flow structure due to the 3D effects. The simulation results of rhoCentralFoam for over-expanded SERN flow were not ideal. The Fluent can produce physical solutions, and it achieved limited success. The existing errors were mainly caused by the inlet boundary setting.

**Keywords:** fluent; rhoCentralFoam; SERN; overexpanded; RANS



**Citation:** Chen, Y.; Hou, Z.; Zhu, B.; Guo, Z.; Xu, B. Validation for Aerodynamic Performance on Over-Expanded State of Single Expansion Ramp Nozzle Configuration. *Aerospace* **2022**, *9*, 715. <https://doi.org/10.3390/aerospace9110715>

Academic Editor: Pietro Catalano

Received: 9 October 2022

Accepted: 11 November 2022

Published: 14 November 2022

**Publisher's Note:** MDPI stays neutral with regard to jurisdictional claims in published maps and institutional affiliations.



**Copyright:** © 2022 by the authors. Licensee MDPI, Basel, Switzerland. This article is an open access article distributed under the terms and conditions of the Creative Commons Attribution (CC BY) license (<https://creativecommons.org/licenses/by/4.0/>).

## 1. Introduction

A single expansion ramp nozzle (SERN) with an asymmetric configuration is usually applied as the exhaust component of scramjet engines. The SERN can achieve the requirement of airframe/propulsion integration by using the vehicle afterbody as part of its upper expansion ramp [1]. As one of the significant parts of the scramjet, the SERN should be adaptive to variations of a wide range of flight conditions [2,3]. The SERN operates at imperfectly expanded conditions, especially over-expanded conditions, resulting in the degradation of the SERN performance.

Many studies have attempted to achieve better performance of the SERN working in over-expanded conditions [2,4–8]. The results show that the SERN performance is greatly influenced by flow separation phenomena and shock motions. The main separation pattern is the restricted shock separation (RSS) and the free shock separation (FSS) in overexpanded SERN [4–6]. The shock train is also commonly found at over-expanded operations, including incident shock, reflected shock, Mach disc, etc. The complex flow field feature can deteriorate the performances of the SERN, especially the lift force. Moreover, the shock train and separation pattern travel along a different path during upstream and downstream movements at startup and shutdown processes, which leads to a hysteresis loop of the SERN performance [9,10].

From the preceding descriptions, there has been coherent effort to understand the SERN flow field for various pressure ratios and geometries or its effect on the performance

parameters of the SERN. Numerical methods were applied to achieve a more detailed flow field for aiding design and measuring the performance of the SERN [11,12]. Scholars tend to use the robust, mature commercial Fluent solver [10,13] to understand the flow behavior of the SERN in a comprehensive manner. Recently, many studies focusing on the OpenFOAM toolkit have been published [14–16], which shows that OpenFOAM has superior accuracy and stability. Marcantoni et al. [17] found that rhoCentralFoam, a density-based compressible turbulence solver based on the central-upwind scheme of Kurganov and Tadmor, could capture normal and oblique shock waves in supersonic flows at 5 Ma. Zang et al. [18] used rhoCentralFoam to simulate round supersonic free jets under various working conditions. Their results showed that rhoCentralFoam has certain advantages over commercial software in solving such problems.

However, most efforts have only attained limited success. Actually, there are many difficulties associated with validating numerical methods of the SERN at an over-expanded state [6,19]: (1) prediction of the separation point; (2) inlet conditions that are difficult to simulate; (3) experimental conditions that are difficult to simulate; (4) 3D and 2D effects; and (5) RANS models lack accuracy at high jet velocities. The purpose of this paper is to establish an accurate numerical simulation process to determine the aerodynamic performance of the SERN at over-expanded conditions. The verification process involves two solvers, which are ANSYS Fluent v202 and OpenFOAM v8. The rationality of the numerical method is verified by comparing the calculated data with the experimental data.

The sections of this paper are arranged as follows: First, the numerical methods adopted by the Fluent and rhoCentralFoam solvers and the geometric configuration of the SERN are briefly introduced. Subsequently, the boundary conditions and grid settings used in this study are described, and the grid independence analysis is discussed. The results analysis includes the following content: (a) the 2D and 3D wall pressure simulation results using Fluent and the 2D wall pressure simulation results using rhoCentralFoam are respectively compared; (b) the impact of 2D and 3D simulations of the Fluent solver on capturing the jet shock wave structure is qualitatively and quantitatively analyzed; (c) the influence of the 2D and 3D simulations on the mixing characteristics of shear layer development; and (d) the numerical and experimental results of aerodynamic performance parameters are compared. Finally, a summary is presented.

## 2. Numerical Method

This study first verified the capability of the commercial software, Ansys Fluent v202, to simulate the jet flow field and performance characteristics of the SERN. Later, we verified the capability of the rhoCentralFoam solver in the open-source CFD toolbox OpenFOAM v8 to simulate the above problems. References [18,20–22] were the main source for the setup of the computations performed in the present study. The OpenFOAM and Fluent solvers used in this study were not modified. Therefore, we only briefly introduced the numerical methods.

### 2.1. Roe-FDS Solver

The Fluent solver selected in this work is a steady-state density-based solver. The numerical method used was based on the finite volume method. The compressible RANS equation was used for modeling an SERN jet. Gravity and body forces were ignored. The working fluid was set as the ideal gas. The viscosity coefficient  $\mu$  was calculated using the Sutherland transport model [21]. The  $k - \omega$  SST model has demonstrated reliability in various numerical simulation studies of transonic and supersonic flow [23–25]. Therefore, in this study, the  $k - \omega$  SST model was used to calculate the eddy viscosity coefficient  $\mu_t$ . The second-order upwind scheme was used to calculate the convection term, and Roe-averaged flux difference splitting (Roe-FDS) was used to calculate the flux [22]. We denoted the Fluent solver used in this study by 'Roe-FDS'. An implicit algorithm was used to solve the time marching equation.

## 2.2. RhoCentralFoam Solver

rhoCentralFoam is an explicit density-based solver that supports polyhedral mesh. The unsteady Reynolds-averaged Navier–Stokes (URANS) equations, which include the mass, momentum, and energy conservation equations, are solved based on the finite volume approach. The physical property settings of the gas were similar to those in the Fluent cases. The working fluid was chosen as the ideal gas. The molecular viscosity coefficient  $\mu$  is calculated using the Sutherland transport model, and the  $k - \omega$  SST turbulence model was used to calculate the eddy viscosity coefficient  $\mu_t$ . Numerical flux at the grid interface was calculated based on the central-upwind schemes of Kurganov and Tadmor [26,27]. The total variation diminishing (TVD) scheme with the van Leer limiter was used to interpolate the state variables on the cell faces to suppress the non-physical oscillation near discontinuities in compressible flows and capture shockwaves relatively accurately. The physical time  $\Delta t$  was set as  $1 \times 10^{-9}$  s and limited such that the maximum Courant number did not exceed 0.5.

## 3. Numerical Setup

### 3.1. Description of the Target Experiment

The SERN configuration used in this study was obtained from the experimental study conducted by Yazhini and Kathiravan [28] in 2021. A working SERN model was mounted at the end of a settling chamber using a nozzle adaptor, as shown in Figure 1. The flow exited into the atmosphere. Through qualitative and quantitative comparisons between the numerical simulation and experimental results, the accuracy and reliability of the Roe-FDS and rhoCentralFoam solvers were confirmed.

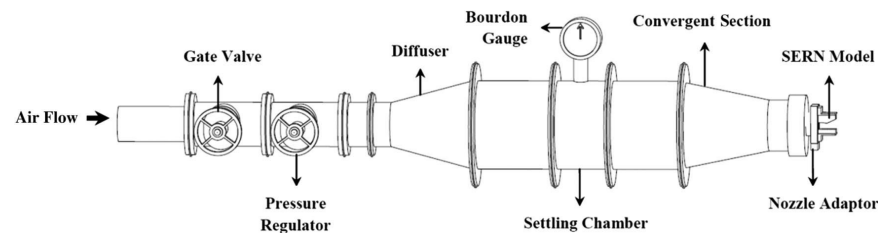


Figure 1. Schematic representation of the open jet facility [28].

The SERN configuration is shown in Figure 2a. The coordinate origin  $(0, 0, 0)$  was set at the center of the nozzle inlet. The inlet height was  $H_{in} = 20$  mm, the throat height was  $H_t = 18$  mm, and the outlet height was  $H_{out} = 30.31$  mm. The length of the constant area of the nozzle inlet was  $L_{const} = 15$  mm. The length of the convergent part of the ramp was  $L_{div} = 11$  mm, and the convergent angle of the ramp was  $\theta_1 = 10.3^\circ$ . The length of the divergent part of the ramp was  $L_{conv} = 26.4$  mm, and the divergent angle of the ramp was  $\theta_2 = 25^\circ$ . The lower surface of the nozzle remained horizontal. The cross-section of the nozzle was rectangular with a width of  $W = 30$  mm; see Figure 2b.

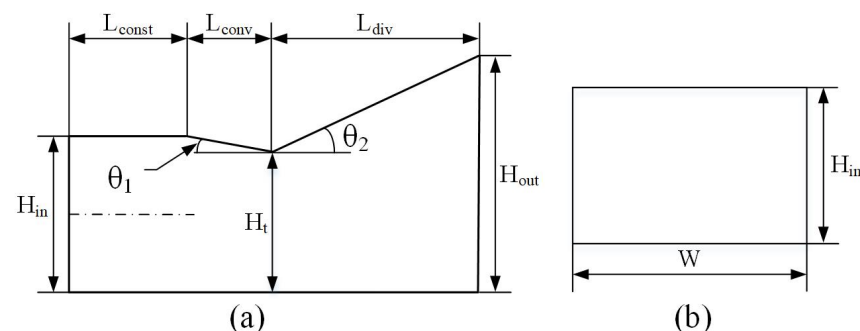


Figure 2. Sketch of the SERN. (a) Configuration of the SERN; (b) Injection section.

### 3.2. Boundary Condition

Yazhini and Kathiravan [28] conducted their experiment for NPRs ranging from 1.5 to 9. The expression for NPR and its relation to jet Mach number  $Ma_j$  are illustrated in Equation (1) [18].  $P_0$  was the total pressure at the nozzle inlet, and the ambient pressure was  $P_a = 101,325$  Pa. The specific heat ratio was  $\gamma = 1.4$ , the total temperature was  $T_0 = 300$  K, and the gas constant was  $R = 287$  kJ/(kg · K). The design jet Mach number was  $Ma_d = 2$ , and the design NPR of the SERN was  $NPR_d = 7.82$ .

For the Roe-FDS solver, the nozzle inlet condition was set as the pressure-inlet, as shown in Figure 3a. The total temperature and total pressure were as described previously. The free flow inflow surface as well as the lateral and downstream outflow surfaces were set as the pressure-far-field boundary condition. The inner and outer walls of the nozzle were set as the no-slip and adiabatic wall boundary conditions which means the local heat flux through the surface of the wall was taken as zero. For the rhoCentralFoam solver, the total temperature and total pressure [20] at the nozzle inlet were equal to those from the Roe-FDS solver. The adopted far-field boundary was the waveTransmissive boundary condition, which guarantees that fluid and sound waves will flow smoothly out of the domain through the boundary; this prevents the boundary reflections from affecting the solutions. The types of OpenFOAM boundary conditions are listed in Table 1.

$$NPR = \frac{P_0}{P_a} = \left(1 + \frac{(\gamma - 1)}{2} Ma_j^2\right)^{\frac{\gamma}{\gamma - 1}} \quad (1)$$

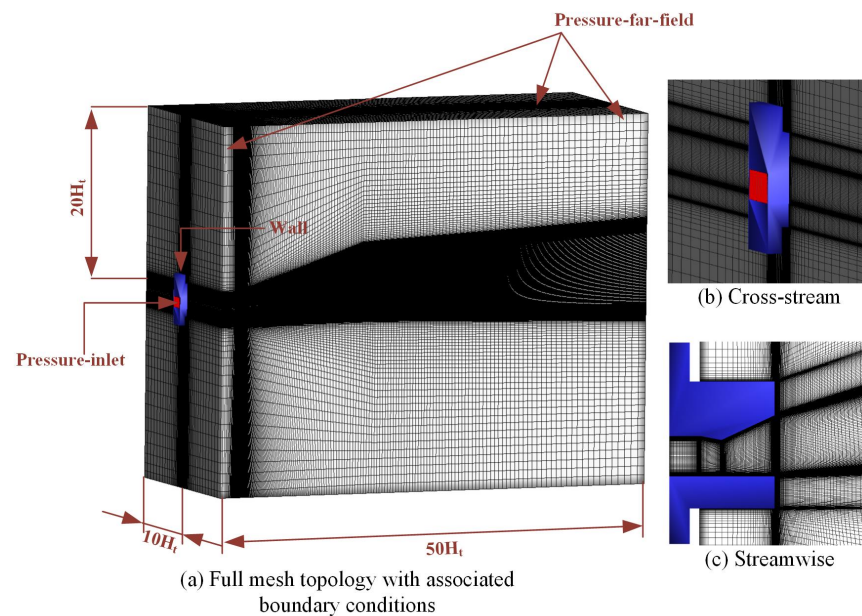


**Figure 3.** Three-dimensional mesh topology for the present SERN jet with (a) boundary conditions; (b) zoomed-in view on cross-stream grid. (c) zoomed-in view on streamwise grid.

**Table 1.** Boundary conditions for the numerical simulations of SERN jet flows using rhoCentralFoam.

Boundary Types	SERN Inlet	Far-Field	Wall
$p$ (kg/(m · s <sup>2</sup> ))	totalPressure	waveTransmissive	zeroGradient
$U$ (m/s)	zeroGradient	waveTransmissive	noSlip
$T$ (K)	totalTemperature	zeroGradient	zeroGradient

### 3.3. Mesh Topology

As shown in Figure 3, the grid topology of the SERN computational domain extended from the nozzle inlet along the streamwise direction, downstream for approximately  $50H_t$  (50 times the throat height); see Figure 3a. In the longitudinal and span-wise directions, the computational domain extended from the nozzle wall to the  $20H_t$  and  $10H_t$  far fields, respectively. The grid construction method was the one adopted by Zang et al. [18] and Yang et al. [29] in the studies of supersonic free jets. In Figure 3a, it is shown that the topology was divided into two different areas, a relatively coarse outer area and a dense core area. The shear layer in the dense core area was further refined to better capture the mixing characteristics of the jet shear layer. In addition, it was ensured that the grid growth factor in the whole computational domain did not exceed 1.2 to prevent unnecessary numerical instability due to abrupt changes in grid size between adjacent cells.

## 4. Results and Discussion

### 4.1. Mesh Independence Study

To evaluate the solver more comprehensively, the symmetry plane (2D) and full computational domain (3D) of the SERN were simulated in this study to exclude any possible 3D effects of the nozzle sidewall. A portion of the 2D mesh along the nozzle symmetry plane is shown in Figure 3c. The grid independence was studied to reduce the impact of grid resolution on the final simulation results. Grid independence analysis is conducted with the following node distributions:  $6.9 \times 10^6$  nodes (coarse),  $9.6 \times 10^6$  nodes (medium), and  $1.5 \times 10^7$  nodes (fine). Table 2 shows the specific parameters of grid settings. Regardless of whether the grid was refined, the height of the first grid layer on the nozzle wall was always set to  $1.5 \times 10^{-6}$  m to guarantee the  $y^+ \approx 1$  requirement of the  $k - \omega$  SST turbulence model. The growth factor of the boundary layers was no more than 1.15, and more than 20 cells were allocated in the viscous sub-layer.

**Table 2.** Grid settings of the computational models.

Case	$N_x$	$N_y$	$N_z$	Cell Number
3D coarse	176	244	119	$6.9 \times 10^6$
3D middle	216	299	146	$9.3 \times 10^6$
3D fine	243	345	168	$1.5 \times 10^7$
2D middle	216	299	-	$6.4 \times 10^4$

This study focused on steady-state (or fully developed) solutions. Furthermore, the implicit solver can use a large time step to obtain the convergence solution, which is efficient. Therefore, Roe-FDS was used to conduct the grid independence research. The working condition of  $NPR = 5$  was selected as the test case, and the supersonic jet flow was in a weak over-expanded state ( $NPRd = 7.82$ ). The convergence criteria were taken from studies by Zang et al. [18]. The jet convection from the nozzle outlet to the end of the computational domain, and the discrepancy in the mass flow rate between the inlet and outlet, was less than 0.1%. Consequently, the numerical results converged.

The pressure distributions on the ramp with different grids are shown in Figure 4. The measured wall static pressures  $p$  were non-dimensioned with the nozzle inlet  $p_0$  and plotted against the length along ramp  $x$  normalized by throat height  $H_t$ . The results show that the differences between the 3D medium and fine grids are considerably small, and the maximum difference is within 1.0%. The pressure distributions of coarse grids on the SERN convergence section showed subtle differences from those of the other two 3D meshes. Therefore, the medium grids were used for numerical simulations as a reasonable compromise between the computational resource and calculation precision.

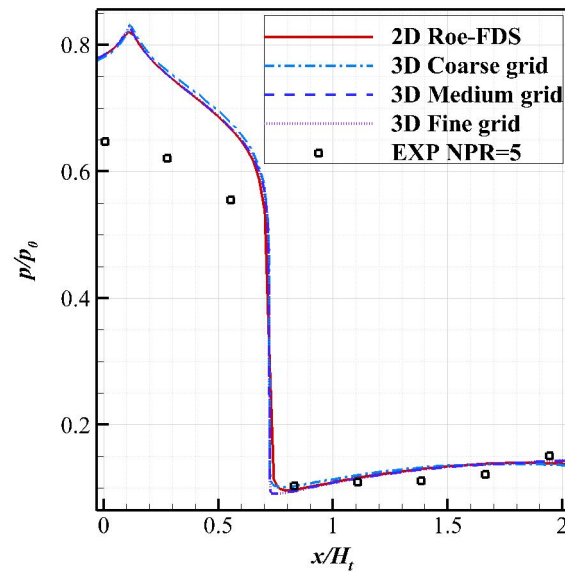


Figure 4. Pressure distributions of different grids on the ramp centerline surface at NPR = 5.

In addition, good agreements can be observed between the 2D and 3D simulation results, suggesting that there is not much change in pressure distributions due to three-dimensional effects, which was consistent with the results of Papamoschou et al. [30] and Tsunoda et al. [31]. However, the four meshes overestimated the static pressure on the converging section from the experimental results. It is clear that the source of the discrepancy in the data is not the solvers or the meshes themselves. The following sections will continue this discussion in depth. The test cases in the following sections are listed in Table 3.

Table 3. A summary of the test cases.

Case	Grid Independence Study	Wall Pressure Distributions	Shock Wave Structure	Shear Layer Development	SERN Performance
NPR	5	1.5, 3, 4, 8	3, 4, 8	3, 4, 8	1.5–9
Roe-FDS	2D, 3D	2D, 3D	2D, 3D	2D, 3D	2D
rhoCentralfoam	-	2D	-	-	-

#### 4.2. Wall Pressure Distributions

From over-expanded to fully expanded flow, the SERN jet needs to go through four critical conditions, NPR = 1.5, 3.0, 4.0, and 8.0.

##### 4.2.1. Roe-FDS Results

Figure 5 shows a comparison of the static pressures on the upper wall of the nozzle in the experiment and numerical simulation. In the experimental study of Yazhini et al. [28], wall static pressure distributions along the centerline of the SERN were measured. The first pressure measuring point was located 1 mm upstream of the convergence section. This position was defined as  $x/H_t = 0$ . The throat was located at  $x/H_t = 0.722$ . The pressure distribution data from the present simulations are taken in section  $z = 0$ . The location definition of the pressure calculation data is consistent with the location definition of the measurement points by Yazhini et al. [28]. The calculation made by the Roe-FDS solver similarly overestimated the wall pressure at the convergence section of the SERN at the four NPRs, particularly at NPR = 1.5, which resulted in the overestimation of the static pressure and shock wave strength downstream.

The overestimated pressure trend existed in all cases. It is possible that the experimental data contain errors or were incorrectly processed. Because the nozzle flow occurs at sufficiently high pressure levels, 1D isentropic estimations can be applied here. Using area–Mach number relation [32] and the nozzle dimensions, it can be derived that at the nozzle inlet, the pressure ratio  $p/p_0$  should be about 0.735, at least for  $\text{NPR} > 5$ . This value is close to the value obtained in the numerical simulation and differs significantly from the experimental value.

Another reason for the difference between the numerical and experimental data may be derived from the lack of rationality of the inlet boundary conditions settings. The total pressure inlet was chosen based on the assumption that the upstream of the nozzle inlet is a stable high-pressure air reservoir with zero flow rate. However, the nozzle adapter mounted between the SERN model and the settling chamber might have caused the total pressure loss, as shown in Figure 1. Using the gauge pressure measured in the settling chamber as the boundary condition of the SERN model may overestimate the inlet pressure. The numerical simulation included the upstream test device, and that probably improved the accuracy of the prediction of the flow behaviors inside the SERN. Unfortunately, Yazhini and Kathiravan [28] did not provide the geometric models of the settling chamber and nozzle adapter.

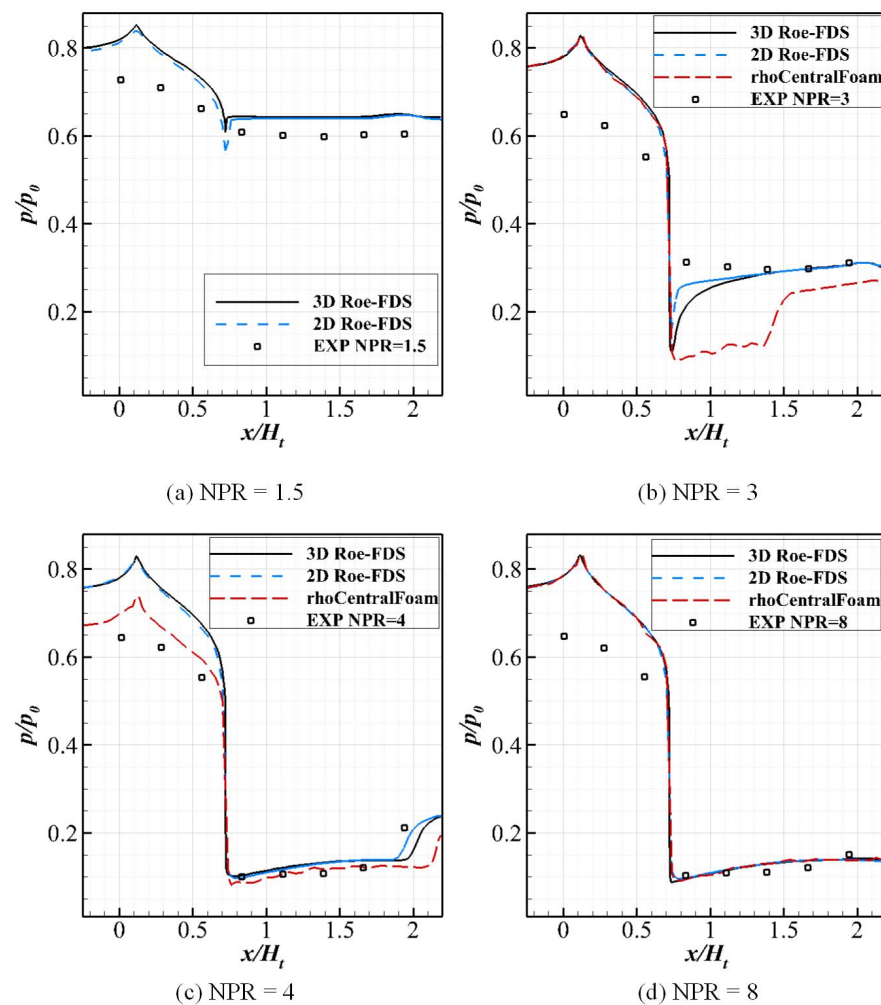


**Figure 5.** Comparison of the pressure on the ramp between the numerical simulation and experimental measurements [28]. (a)  $\text{NPR} = 1.5$ , high subsonic separated pipe flow; (b)  $\text{NPR} = 3$ , flow attached to the starting point of the ramp wall; (c)  $\text{NPR} = 4$ , the jet is almost fully attached to the ramp wall; (d)  $\text{NPR} = 8$ , fully expanded jet.

The 3D effects of the flow inside the SERN were weak. The existence of the side wall in 3D computations limited the lateral expansion of the flow in the nozzle. Hence, the flow field profile along the spanwise direction demonstrated almost the same, which reduced the 3D effects. The differences between the 2D and 3D simulations mainly resulted from the 3D vortical structures because the deviations mainly occurred in the separation area at the corner or after shocks, as shown in Figure 5a–c. Furthermore, the 2D results were in agreement with 3D results at NPR = 8 operating condition without the detached flow; see Figure 5d. Therefore, 2D CFDs are sufficient to predict wall static pressure data on the SERN wall.

#### 4.2.2. rhoCentralFoam Results

To save computing resources, the rhoCentralFoam case only performs the 2D simulation. It cannot produce accurate solutions at low blowing rates (i.e., NPR = 1.5, 3 and 4). The solution at NPR = 1.5 was non-physical and not well-converged. Thus, the rhoCentralFoam results at NPR = 1.5 are not plotted in Figure 5a. The results for NPR = 3 and 4 were quite different from those in the experiment and the Reo-FDS simulation; see Figure 5b,c. However, the solution by rhoCentralFoam was highly consistent with that of the Reo-FDS at NPR = 8; see Figure 5d. The calculation made by the rhoCentralFoam also overestimated the inflow pressure for each case, further proving that the settings for the total pressure boundary were unreasonable.

When NPR was <4, low-speed detached flow was noted in the SERN. The inaccurate solutions derived by rhoCentralFoam at low blow rates may be because of its inability to solve flows at all speed regimes. The limitations of rhoCentralFoam are inherently tied to the flux scheme employed. Using a standard compressible code to calculate low-speed flows was not ideal, which was a finding also mentioned in the study by Liou [33]. Because the rhoCentralFoam simulation for the SERN wall pressure lacked numerical stability and accuracy, only Reo-FDS results were used for subsequent research.

#### 4.3. Shock Wave Structure

Figure 6 shows a comparison between the experimental and numerical schlieren images. The processing method of numerical schlieren images can be found in references [34–36]. They show details of the shock wave structures with NPR = 3, 4, and 8. The poor solutions at NPR = 1.5 are not discussed in this section. Furthermore, we also drew the Mach contour-assisted wave pattern explanations in the jet, as shown in Figure 7.

The 2D simulation results accurately described the internal flow pattern of the SERN; however, the wave structure in the external supersonic jet core was quite different from that in the experimental schlieren image. The shock waves were marked with blue arrows, which were inconsistent with the experimental schlieren, as shown in Figure 6. The lateral expansion and interactions of the 3D shocks of the jet leaving the outlet of the SERN can be difficult to accurately account for when performing 2D CFD. Therefore, the 2D simulation results were not satisfactory.

The 3D simulation results accurately depict the flow pattern inside and even outside the SERN. Some wave systems that could not be easily identified in the experiment were also present in the 3D simulation (i.e., the Lambda shock wave at NPR = 4 and oblique shock at NPR = 8). We used the distance from the nozzle outlet to the intercepting point of the two shocks to represent the approximate length of the first jet potential core in the 3D simulation; see Figure 6e–g. The distance is normalized by throat height  $H_t$ . Simulations over-predict the first shock cell lengths regardless of the exit conditions by at least 9.1%. The consistent overestimation of the shock cell length in 3D numerical simulations can be attributed to the aforementioned unreasonable inlet boundary setting, leading to the wave system in the shock cell to be pushed farther downstream of the outlet.

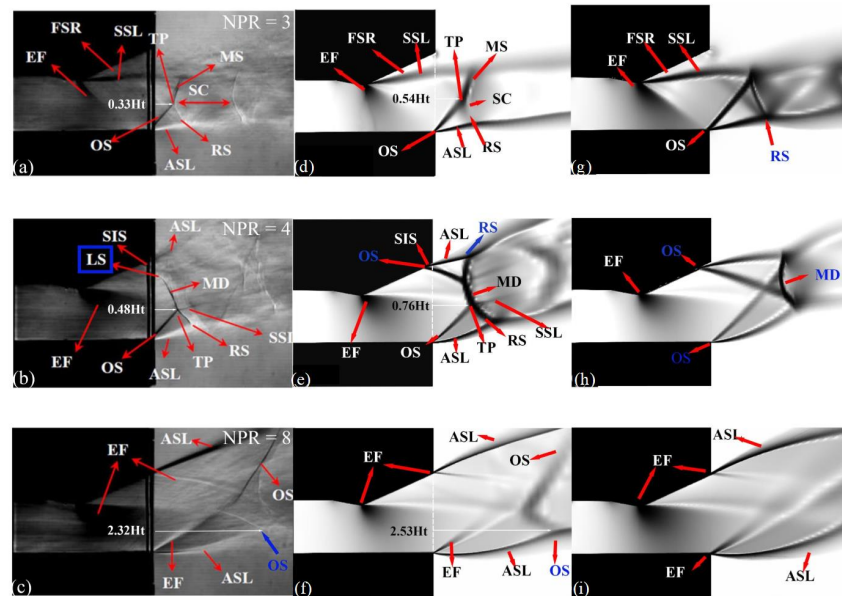


**Figure 6.** Schlieren and numerical flow visualization images at NPR = 3, 4, and 8. (a–c) Experimental schlieren measurement; (d–f) Three-dimensional numerical Schlieren contours; (g–i) Two-dimensional numerical schlieren contours. ASL denotes the atmospheric shear layer, EF denotes the expansion fan, MD denotes the Mach disc, OS denotes the oblique shock, TP denotes the triple point, SSL denotes the separated shear layer, FSR denotes the flow-separated region, CS denotes the curved shock, RS denotes the reflected shock, SIS denotes the shock-induced separation, and LS denotes the lambda shock.

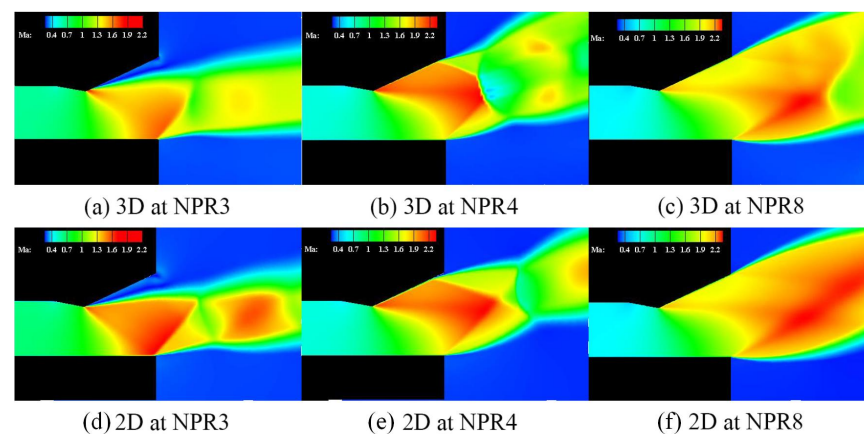


**Figure 7.** Near-field shock structures of the supersonic jet flows at NPR = 3, 4 and 8.

#### 4.4. Shear Layer Development

The mixing characteristics of the free jet shear layer can be accurately measured and investigated through flow quantities such as the turbulent kinetic energy (TKE) or Reynolds stress [18]. Fortunately, the  $k - \omega$  SST model can directly evaluate the turbulent kinetic energy  $k$  and specify the output during the solving process. Owing to the constraints of the experimental technology, it was difficult to obtain a highly accurate turbulent kinetic energy in the experiment. The jet width is the distance between the shear layers on both sides of the jet axis, which can be used to measure the jet expansion rate or momentum flux distributions to verify the numerical results. The jet width can also be estimated from the numerical results of the turbulent kinetic energy.

The jet width was measured manually with an outlining criterion at 10% of the maximum TKE in the numerical schlieren. The nozzle throat height was set as the reference

length. Two measuring points of the jet width were set for each calculation case, and they were located at  $x/H_t = 1$  and 2 downstream from the tip of the ramp of the SERN, as shown in Figure 8. Tables 4 and 5 show the comparison between the 2D and 3D jet width simulation and experimental results.

The 2D modeling had a difficulty in accurately predicting the jet width of the SERN; this was mainly owing to the difficulty in simulating the shock wave in the jet. Particularly when  $\text{NPR} = 4$ , the wave structure predicted by the 2D simulation was completely inconsistent with the experimental results, which resulted in a difference of nearly 30% in the prediction of the jet width. When  $\text{NPR} = 3$ , the 3D simulation prediction error of the jet width at  $1H_t$  also reached 19.4%, which was caused by the inaccurate estimation of the shock wave position. In general, the 3D simulation outperformed the 2D simulation. Prior quantitative studies of shock wave structures did not deliver ideal results; thus, in this study, it was difficult to evaluate the Reo-FDS code's capability to accurately simulate the shear layer development and mixing characteristics from the jet width. However, the prediction error of other Reo-FDS 3D cases in determining the jet width of the shear layer did not exceed 10%, and they were within an acceptable range.

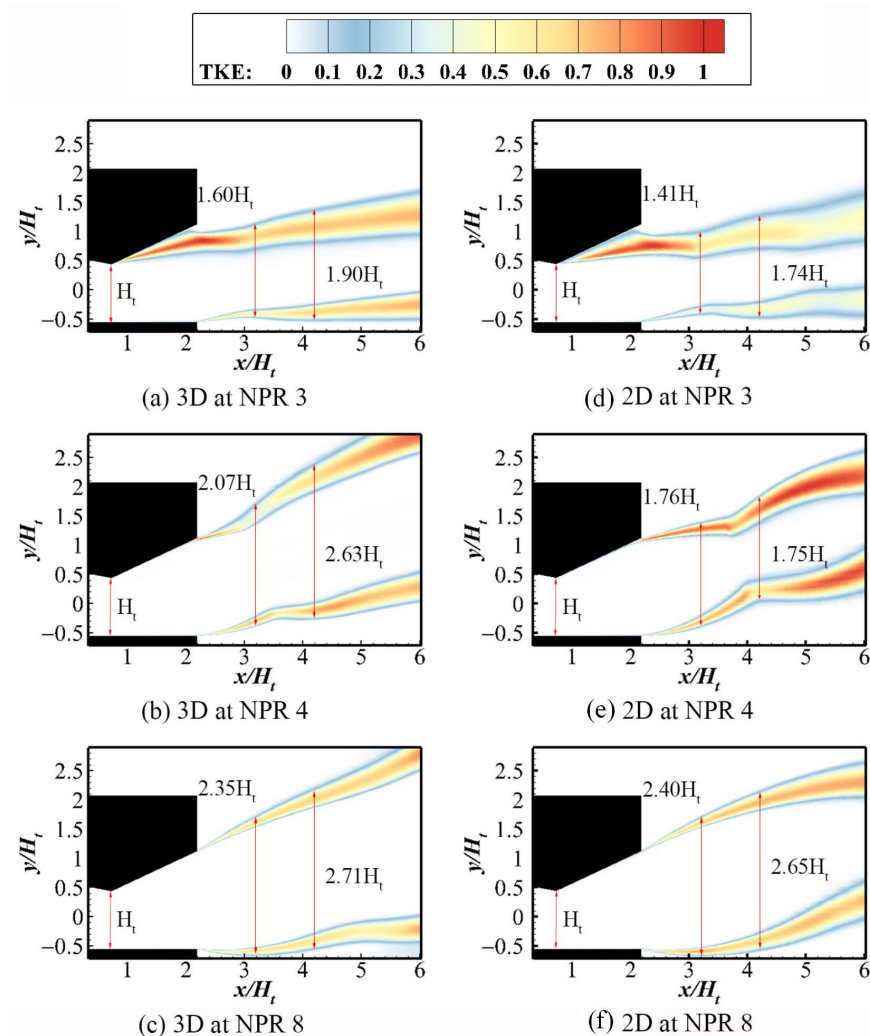


Figure 8. Jet widths at various NPR conditions.

**Table 4.** Jet width at  $1H_t$  location from the exit of the ramp section.

NPR	Jet Width		
	EXP	3D (Discrepancy)	2D (Discrepancy)
3	1.34	1.60 (19.4%)	1.41 (5.2%)
4	2.13	2.07 (−2.8%)	1.76 (−17.3%)
8	2.17	2.35 (8.3%)	2.40 (10.5%)

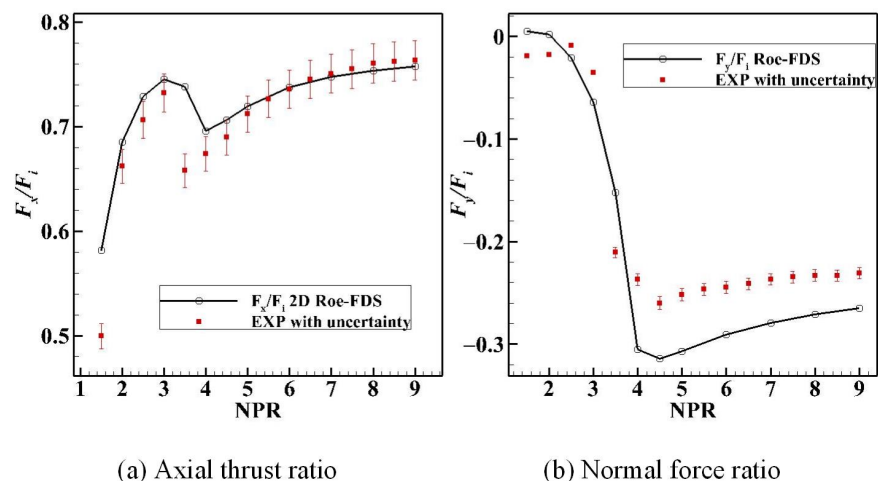
**Table 5.** Jet width at  $2H_t$  location from exit of the ramp section.

NPR	Jet Width		
	EXP	3D (Discrepancy)	2D (Discrepancy)
3	1.77	1.90 (7.3%)	1.74 (−1.7%)
4	2.50	2.63 (5.2%)	1.75 (−30.0%)
8	2.52	2.71 (7.5%)	2.65 (5.1%)

#### 4.5. Comparison of SERN Performance

This section presents an estimate of the aerodynamic performance of the nozzle based on the wall static pressure at the centerline of the SERN with an inlet NPR in the range of 1.5–9. The above analysis showed that there were almost no 3D effects in the SERN attached flow case. Research results of Hirschen et al. [37,38] and Thiagarajan et al. [39] also showed that there was not much change in performance from 2D calculations compared to 3D calculations. To save computing resources, the 2D data will be used to confirm the effectiveness of the force characteristics computing model. The method used to calculate the total thrust  $F_x$ , lift  $F_y$ , ideal thrust  $F_i$  and moment coefficient  $C_m$  was like that of Yazhini and Kathiravan [28].

Figure 9 presents a comparison of the changes in the  $F_x/F_i$  and  $F_y/F_i$  with increasing NPR between the experimental data and the present CFD results. The moment coefficient  $C_m$  was mainly affected by the lift  $F_y$ , which had the same change trend as  $F_y/F_i$  and the experimental test results, as shown in Figure 10. The main deviation occurred when NPR ranged from 3 to 4. At this time, the shock wave was pushed downstream in the SERN, and the shock wave train showed significantly unsteady characteristics. It was difficult for the solver to accurately capture the shock wave position. The deviation also occurred with  $NPR < 3$ . This was mainly caused by the error of the overestimated inlet static pressure propagating downstream before nozzle choking. However, the current numerical methods captured the changing trend in the force characteristics with the increase in NPR, which means the current numerical methods achieved limited success.

**Figure 9.** Comparisons of axial thrust ratio and normal force ratio at various NPR conditions.

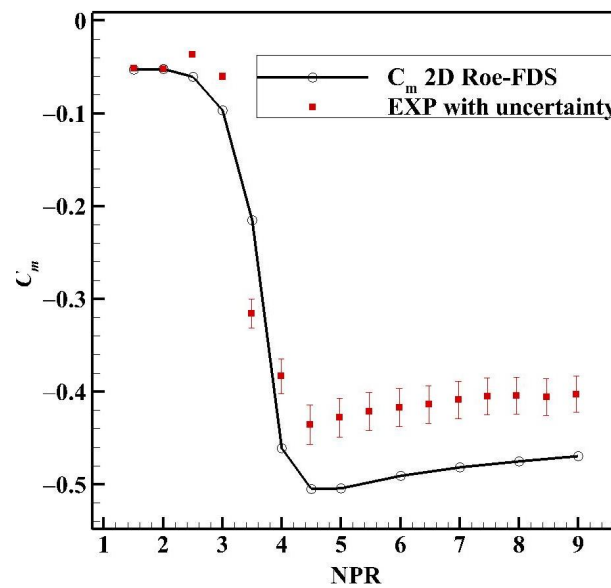


Figure 10. Comparisons of the coefficient of pitching moment at various NPR conditions.

## 5. Conclusions

In this study, a RANS simulation of the SERN jet in an over-expanded state was conducted using the Reo-FDS and the rhoCentralFoam solvers in OpenFOAM. To evaluate the numerical stability and accuracy of the two solvers, the grid independence analysis is discussed. The wall pressure distributions and flow field characteristics were studied in detail with an inlet NPR of 1.5, 3, 4, and 8. The SERN aerodynamic performance with an inlet NPR ranging from 1.5 to 9 was then calculated.

Relative to the experimental results, Reo-FDS overestimated the wall pressure, shock wave strength, and shock wave position; this overestimation was mainly caused by the inappropriate setting of the inlet condition. The simulation capability of the 2D model for the pressure distributions on the SERN wall matched that of the 3D model, and the 3D effects were weak. The rhoCentralFoam solver failed to simulate the high subsonic performance and predict the shock separation phenomena. The rhoCentralFoam simulation results for over-expanded complex flow inside SERN were not ideal.

Subsequently, the width of the jet as well as the approximate length of the jet potential core were found on the near-field shock structures using the Reo-FDS. Comparing the flow field simulation results with the experimental schlieren, the Reo-FDS 3D can predict the flow behavior inside and outside the nozzle qualitatively because the 3D simulation results overestimated the distance length of the jet potential core due to the overestimation of the inlet pressure. The 2D modeling can accurately simulate the internal flow field of the nozzle but fails to predict the external flow structure due to the 3D effects.

For NPR = 1.5–9, the trend of the calculated SERN aerodynamic performance by Reo-FDS was consistent with the experimental results. The difference was mainly caused by the overestimation of the nozzle inlet pressure and the difficulty in capturing the separation position in the convergent section using the current calculation methods.

Reo-FDS had a physical solution when simulating the complex flow in the over-expanded state of the SERN and could be used to qualitatively study such problems using current numerical methods. The reason for the errors under different operations was the lack of rationality in the setting of the inlet boundary conditions. In the future, incorporating the test equipment upstream of the nozzle in the geometric model can be considered; it is expected that good simulation results will be achieved with this configuration.

**Author Contributions:** Conceptualization, Y.C., Z.H. and Z.G.; methodology, Y.C.; validation, Y.C.; writing—original draft preparation, Y.C., B.Z., Z.G. and B.X.; writing—review and editing, Y.C. and B.X.; visualization, Y.C.; supervision, B.Z. and Z.G.; funding acquisition, B.Z. All authors have read and agreed to the published version of the manuscript.

**Funding:** This research was funded by the National Natural Science Foundation of China, grant number 52172410 and 61903369.

**Data Availability Statement:** Not applicable.

**Conflicts of Interest:** The funders had no role in the design of the study; in the collection, analyses, or interpretation of data; in the writing of the manuscript, or in the decision to publish the results.

## Abbreviations

The following abbreviations are used in this manuscript:

RANS	Reynolds-averaged Navier–Stokes
NPR	Nozzle pressure ratio
CFD	Computational fluid dynamics
$k - \omega$ SST model	$k - \omega$ shear stress transport turbulence model
TKE	Turbulent kinetic energy

## References

- Laiton, S.N.P.; Martos, J.F.D.; Rego, I.D.; Marinho, G.S.; Toro, P.G.D. Experimental Study of Single Expansion Ramp Nozzle Performance Using Pitot Pressure and Static Pressure Measurements. *Int. J. Aerosp. Eng.* **2019**, *2019*, 7478129. [\[CrossRef\]](#)
- Hindash, I.O.; Spaid, F.W. CFD validation and wind tunnel test for a NASP single expansion ramp nozzle in the transonic regime. In Proceedings of the 29th Aerospace Sciences Meeting, Reno, NV, USA, 7–10 January 1991.
- Lv, Z.; Xu, J.; Yu, K.; Song, G. Experimental and numerical investigations of a scramjet nozzle at various operations. *Aerosp. Sci. Technol.* **2020**, *96*, 105536. [\[CrossRef\]](#)
- Yu, Y.; Xu, J.; Yu, K.; Mo, J. Unsteady transitions of separation patterns in single expansion ramp nozzle. *Shock Waves* **2015**, *25*, 623–633. [\[CrossRef\]](#)
- He, C.; Li, J.; Fan, Z. Flow separation unsteadiness in single expansion ramp nozzle. *J. Aerosp. Power (Chinese)* **2019**, *34*, 2339–2346.
- Yu, Y.; Xu, J.; Mo, J.; Wang, M. Numerical Investigation of Separation Pattern and Separation Pattern Transition in Overexpanded Single Expansion Ramp Nozzle. *Aeronaut. J.* **2014**, *118*, 399–424. [\[CrossRef\]](#)
- Lv, Z.; Xu, J.; Mo, J. Numerical investigation of improving the performance of a single expansion ramp nozzle at off-design conditions by secondary injection. *Acta Astronaut.* **2014**, *133*, 233–243. [\[CrossRef\]](#)
- Mousavi, S.M.; Pourabidi, R.; Goshtasbi-Rad, E. Numerical investigation of over expanded flow behavior in a single expansion ramp nozzle. *Acta Astronaut.* **2018**, *146*, 273–281. [\[CrossRef\]](#)
- Jiao, X.; Chang, J.; Wang, Z.; Yu, D. Periodic forcing of a shock train in a scramjet inlet-isolator at overspeed condition. *Acta Astronaut.* **2018**, *143*, 244–254. [\[CrossRef\]](#)
- Qin, B.; Chang, J.; Jiao, X.; Bao, W.; Yu, D. Numerical investigation of the impact of asymmetric fuel injection on shock train characteristics. *Acta Astronaut.* **2018**, *105*, 66–74. [\[CrossRef\]](#)
- Mo, J.; Xu, J.; Quan, Z.; Lv, Z. Design and cold flow test of a scramjet nozzle with nonuniform inflow. *Acta Astronaut.* **2015**, *108*, 92–105. [\[CrossRef\]](#)
- Zhang, P.; Xu, J.; Quan, Z.; Mo, J. Effects of nonuniform Mach-number entrance on scramjet nozzle flowfield and performance. *Acta Astronaut.* **2016**, *129*, 201–210. [\[CrossRef\]](#)
- Xu, K.; Chang, J.; Zhou, W.; Yu, D. Mechanism and Prediction for Occurrence of Shock-Train Sharp Forward Movement. *AIAA J.* **2016**, *54*, 1403–1412. [\[CrossRef\]](#)
- Zang, B.; Vevek, U.S.; New, T.H. OpenFOAM based numerical simulation study of an underexpanded supersonic jet. In Proceedings of the 55th AIAA Aerospace Sciences Meeting, Grapevine, TX, USA, 9–13 January 2017.
- Shen, C.; Sun, F.; Xia, X. Analysis on capabilities of density-based solvers within OpenFOAM to distinguish aerothermal variables in diffusion boundary layer. *Chin. J. Aeronaut.* **2013**, *26*, 1370–1379.
- Shen, C.; Sun, F.; Xia, X. Implementation of density-based solver for all speeds in the framework of OpenFOAM. *Comput. Phys. Commun.* **2014**, *185*, 2730–2741. [\[CrossRef\]](#)
- Marcantoni, L.F.G.; Tamagno, J.; Elaskar, S.A. High Speed Flow Simulation Using openFOAM. In Proceedings of the Mecánica Computacional, Salta, Argentina, 13–16 November 2012.
- Zang, B.; Vevek, U.S.; Lim, H.; Wei, X.; New, T.H. An assessment of OpenFOAM solver on RANS simulations of round supersonic free jets. *J. Comput. Sci.* **2018**, *28*, 18–31. [\[CrossRef\]](#)
- Rumsey, C.L.; Nishino, T. Numerical study comparing RANS and LES approaches on a circulation control airfoil. *Int. J. Heat Fluid Flow* **2011**, *32*, 847–864. [\[CrossRef\]](#)

20. C++ Source Code Guide of OpenFOAM v8. Available online: <https://cpp.openfoam.org/v8/> (accessed on 1 September 2020).
21. Wang, Y.; Xu, J.; Huang, S. Computational study of axisymmetric divergent bypass dual throat nozzle. *Aerosp. Sci. Technol.* **2019**, *86*, 177–190. [[CrossRef](#)]
22. ANSYS. *ANSYS FLUENT Theory Guide*, 17.1; ANSYS Inc.: Canonsburg, PA, USA, 2016.
23. Ju, S.; Yan, C.; Wang, X.; Qin Y.; Ye Z. Effect of energy addition parameters upon scramjet nozzle performances based on the variance analysis method. *Aerosp. Sci. Technol.* **2017**, *70*, 511–519. [[CrossRef](#)]
24. Chen, K.; Xu, J.; Qin, Q.; Xiong, W. Design of Thrust-Optimized Scramjet Nozzle and Its Concise Estimation Method. *AIAA J.* **2021**, *59*, 2014–2026. [[CrossRef](#)]
25. Baucoco, A.R.; Shanley, K.T.; Bevis, D. CFD Validation Study for Internal Performance of Advanced SERN Configurations. In Proceedings of the 48th AIAA/ASME/SAE/ASEE Joint Propulsion Conference & Exhibit, Atlanta, GA, USA, 7–10 January 2012.
26. Kurganov, A.; Tadmor, E. New High-Resolution Central Schemes for Nonlinear Conservation Laws and Convection—Diffusion Equations. *J. Comput. Phys.* **2000**, *160*, 241–282. [[CrossRef](#)]
27. Kurganov, A.; Noelle, S.; Petrova, G. Semidiscrete Central-Upwind Schemes for Hyperbolic Conservation Laws and Hamilton-Jacobi Equations. *SIAM J. Sci. Comput.* **2001**, *23*, 707–740. [[CrossRef](#)]
28. Yazhini, V.I.; Kathiravan, B.; Muruganandam, T.M.; Jayaraman, K. Cowl Length Variation on Performance Characteristics of a Single Expansion Ramp Nozzle. *J. Propul. Power* **2021**, *37*, 780–791. [[CrossRef](#)]
29. Yang, J.; Zhang, Y.; Chen, H.; Song F. Flow separation control in a conical diffuser with a Karman-vortex generator. *Aerosp. Sci. Technol.* **2020**, *106*, 106076. [[CrossRef](#)]
30. Papamoschou, D.; Zill, A.; Johnson, A. Supersonic flow separation in planar nozzles. *Shock Waves* **2009**, *19*, 171–183. [[CrossRef](#)]
31. Tsunoda, K.; Suzuki, T.; Asai, T. Improvement of the Performance of a Supersonic Nozzle by Riblets. *J. Fluids Eng.* **2000**, *122*, 585–591. [[CrossRef](#)]
32. Anderson, J.D. *Fundamentals of Aerodynamics*, 6th ed.; McGraw-Hill Education: New York, NY, USA, 2017; p. 702.
33. Liou, M. A sequel to AUSM, Part II: AUSM<sup>+</sup>-up for all speeds. *J. Comput. Phys.* **2006**, *214*, 137–170. [[CrossRef](#)]
34. Wu, M.; Martin, M.P. Direct Numerical Simulation of Supersonic Turbulent Boundary Layer over a Compression Ramp. *AIAA J.* **2007**, *45*, 879–889. [[CrossRef](#)]
35. Tong, F.; Li, X.; Yuan, X.; Yu, C.D. Incident shock wave and supersonic turbulent boundarylayer interactions near an expansion corner. *Comput. Fluids* **2020**, *198*, 104385. [[CrossRef](#)]
36. Chen, Y.; Hou, Z.; Deng, X.; Guo, Z.; Shao, S.; Xu, B. Numerical Study of the Lift Enhancement Mechanism of Circulation Control in Transonic Flow. *Aerospace* **2021**, *8*, 311. [[CrossRef](#)]
37. Hirschen, C.; Gülhan, A.; Beck W.H.; Henne, U. Measurement of Flow Properties and Thrust on Scramjet Nozzle Using PressureSensitive Paint. *J. Propul. Power* **2009**, *25*, 267–280. [[CrossRef](#)]
38. Hirschen, C.; Gülhan, A.; Beck, W.H.; Henne, U. Experimental Study of a Scramjet Nozzle Flow Using the Pressure-Sensitive-Paint Method. *J. Propul. Power* **2008**, *24*, 662–672. [[CrossRef](#)]
39. Thiagarajan, V.; Panneerselvam, S.; Rathakrishnan, E. Numerical flow visualization of a Single Expansion Ramp Nozzle with hypersonic external flow. *J. Vis.* **2006**, *9*, 91–99. [[CrossRef](#)]